Double-Bounce Component in Cross-Polarimetric SAR From a New Scattering Target Decomposition

Sang-Hoon Hong, *Member, IEEE*, and Shimon Wdowinski

***Abstract*—Common vegetation scattering theories assume that the synthetic aperture radar (SAR) cross-polarization (cross-pol) signal represents solely volume scattering. We found that this assumption is incorrect based on SAR phase measurements acquired over the South Florida Everglades indicating that the cross-pol radar signal often samples the water surface beneath the vegetation. Based on these new observations, we propose that the cross-pol signal consists of both double-bounce and volume scattering components. The simplest multibounce scattering mechanism that generates cross-pol signal occurs by rotated dihedrals. Thus, we use the rotated dihedral mechanism to revise some of the vegetation scattering theories and develop a four-component decomposition algorithm with single-bounce, co-pol double-bounce, cross-pol double-bounce, and volume scattering components. We tested the new decomposition in both urban and rural environments using RADARSAT-2 quad-pol data sets. The decomposition of the San Francisco area shows higher double-bounce scattering and reduced volume scattering in the urban area with respect to the common three-component decomposition. The decomposition of the rural Everglades area shows that the relation between volume and cross-pol double bounce depends on the vegetation density. Thus, we suggest that, when possible, SAR-based biomass estimate studies should use the volume scattering calculated by our decomposition rather than the cross-pol signal, which also contains a double-bounce component.**

***Index Terms*—Cross-polarization (cross-pol), Everglades, polarimetric decomposition, polarimetric synthetic aperture radar (PolSAR), rotated dihedral mechanism, volume scattering, wetland interferometric SAR (InSAR).**

I. Introduction

POLARIMETRIC synthetic aperture radar (PolSAR) decomposition methods were developed to map land cover according to scattering mechanisms [1]–[13]. The widely used Pauli decomposition is a simple method that represents the main three scattering mechanisms: single bounce, double bounce, and volume scattering [1], [2], [11], [12]. A three-component scattering model proposed by Freeman and Durden has been successfully applied to decompose polarized SAR data into three components according to the main scattering mechanisms under reflection symmetry conditions [3]. In order to account for nonreflection symmetry conditions, Yamaguchi *et al.* added a fourth helix component to their decomposition [7], [8]. Various methods were proposed to estimate the volume scattering component considering nonreflection symmetry condition [14]–[17]. Recently, an extended volume scattering model was discussed using randomly orientated diplane scatterers [18]. More recent decomposition studies also included mathematical operations on the decomposed coherency matrix in order to resolve anomalous values generated by the previous three- and four-decomposition methods [9], [10], [13].

A key issue in all decomposition studies is the relations between cross-polarization (cross-pol) and volume scattering. The first generation of three- and four-component decomposition studies assumed that the cross-pol signal solely reflects volume scattering. Yamaguchi *et al.* noticed that volume scattering in urban areas depends on street orientation with respect to the radar direction of illumination and suggested the rotation of the coherency matrix to reduce the volume scattering component [9]. Lee and Ainsworth, and van Zyl *et al.* also reduced the value of volume scattering in their decompositions in order to eliminate negative powers on some pixels, most frequently in double-bounce scattering power [10], [13]. In all three recent decompositions, volume scattering was reduced due to a mathematical operation on the polarimetric scattering matrix.

In this paper, we present a modified four-component decomposition method based on the coherency matrix that decomposes the cross-pol signal into double-bounce and volume scattering components. Consequently, our decomposition yields in a reduced volume scattering component, similar to the results obtained by the three recent decomposition studies [9], [10], [13]. However, unlike the mathematical approaches used by these studies, our decomposition is based on a physical rational that the cross-pol signal contains scattering from ground surface beneath the vegetation, and hence, this scattering from the ground surface should be explicitly included in the decomposition. Our physical-based approach was developed from SAR phase information as a part of our interferometric SAR (InSAR) studies of vegetated wetlands, which shows an almost identical fringe pattern in all polarization interferograms [19]. In order to explain the physical rational of our decomposition approach, we first present the multipolarization interferograms that indicate a significant contribution of scattering from the ground surface in the cross-pol signal. Then, we present the modified four-component decomposition. Finally, we demonstrate the usefulness of the modified decomposition by applying it to two RADARSAT-2 quad-pol data sets: one acquired over

Manuscript received February 3, 2012; revised July 6, 2012, November 28, 2012, and May 14, 2013; accepted June 10, 2013. This work was supported by NASA Cooperative Agreement NNX08BA43A (WaterSCAPES: Science of Coupled Aquatic Processes in Ecosystems from Space).

S.-H. Hong is with the Satellite Information Research Center, Korea Aerospace Research Institute, Daejeon 305-333, Korea, and also with the Division of Marine Geology and Geophysics, University of Miami, Miami, FL 33149 USA (e-mail: shong@kari.re.kr).

S. Wdowinski is with the Division of Marine Geology and Geophysics, University of Miami, Miami, FL 33149 USA.

Color versions of one or more of the figures in this paper are available online at http://ieeexplore.ieee.org.

Digital Object Identifier 10.1109/TGRS.2013.2268853

0196-2892 © 2013 IEEE. Personal use is permitted, but republication/redistribution requires IEEE permission.
See http://www.ieee.org/publications_standards/publications/rights/index.html for more information.

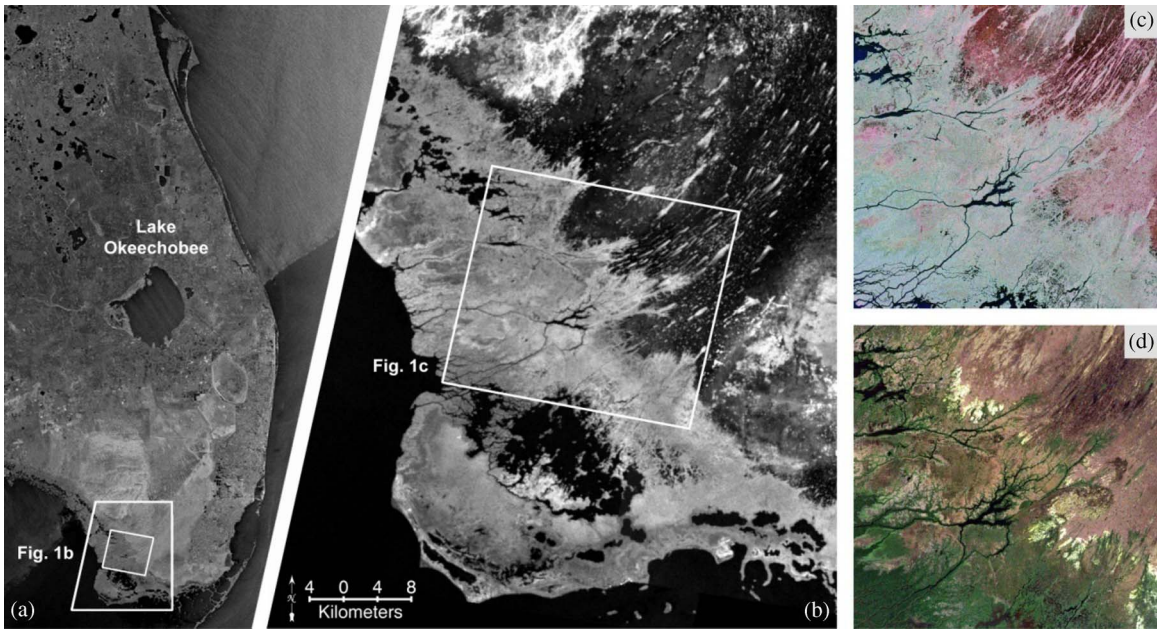

Fig. 1. SAR amplitude images showing the study area in western South Florida. (a) RADARSAT-1 ScanSAR image of Florida showing location of study area (RADARSAT data Canadian Space Agency/Agence Spatiale Canadienne 2002). (b) JERS-1 L-band amplitude image of eastern South Florida showing the location map of the RADARSAT-2 swath. (c) RADARSAT-2 Pauli decomposition color composite image of the study area consisting of saltwater mangrove and freshwater herbaceous wetlands: HH-VV (red), HH+VV (blue), and HV (green). (d) Landsat-7 ETM+ optic color composite image of the study area (http://www.landcover.org/data/landsat/).

the urban environment of San Francisco and the second over the rural Everglades wetlands in South FL, USA.

II. SAR Phase Observations Over Wetlands

A. Wetland InSAR

Wetland InSAR is a relatively recent application of InSAR technology, which measures water-level changes with high resolution in aquatic environment with emergent vegetation [19]–[22]. The method works owing to double-bounce scattering, in which the radar signal backscatters twice, once from the water surface and then by the vegetation, or vice versa [23]. Although most vegetation scattering theories suggest that a short-wavelength SAR signal interacts mainly with the upper sections of the vegetations, our results show that wetland InSAR works well with all wavelength data as long as the time span between the two acquisitions is short (1–100 days, depending on the wavelength) [19], [24]–[27]. Obtaining coherent phase over vegetated area even with short-wavelength repeat orbit InSAR observations suggests that a significant portion of the observed signal is scattered from lower sections of the vegetation that do not move much by wind.

Another unexpected result was found in polarized phase data (interferograms). Our studies have shown an almost identical fringe pattern reflecting surface water-level changes in both co- and cross-polarizations [19], [24]. It is a surprising result because common radar scattering theories assume that cross-pol observations are products of volume scattering corresponding to the interaction between the radar signal and the upper sections of the vegetation. As we show in the following discussion, the similar fringe appearance in the co- and cross-pol interferograms contradicts this assumption.

B. Study Area

The Everglades subtropical wetlands in South FL consist of a wide, shallow, and slow sheet-flow environment. The sheet flow begins in Lake Okeechobee and flows southward to the Everglades wetlands [Fig. 1(a)]. Artificial changes, such as construction of canals and levees in the past half century, have damaged significantly the flow and ecology of the natural wetland system. At present, the Everglades wetland is composed of managed wetlands in the northern section, which is controlled by a series of man-made structures as levees and hydrological gates, and naturally flown wetlands in the southern area, where the original wetland sheet flow has been preserved. In order to maintain the hydrology and ecology of these fragile wetlands, the Everglades wetlands are monitored by a large number of water-level gauges. The large number of stage stations in the area enabled us to verify that the observed phase changes indeed represent water-level changes and to quantify the InSAR measurement uncertainty as 3–5 cm [21], [22], [25].

In this paper, we focus on the southwestern section of the wetlands, which is located in the Everglades National Park [Fig. 1(b)]. This area comprises of various wetland environments across the transition between freshwater and saltwater wetlands as shown in Fig. 1(c). The northeastern part of the study area consists of freshwater herbaceous vegetation [Fig. 2(a)], whereas the southwestern area consists of saltwater woody vegetation (mangroves) as shown in Fig. 2(b). The shorter scrub is developed in the transition zone between freshwater and saltwater comparing with taller and denser mangrove forest in the saltwater wetland (the vegetation map over the Everglades can be found at http://fcelter.fiu.edu/data/GIS). The optical color composite image of Landsat-7 ETM+ (http://www.landcover.org/data/landsat) describes clearly two

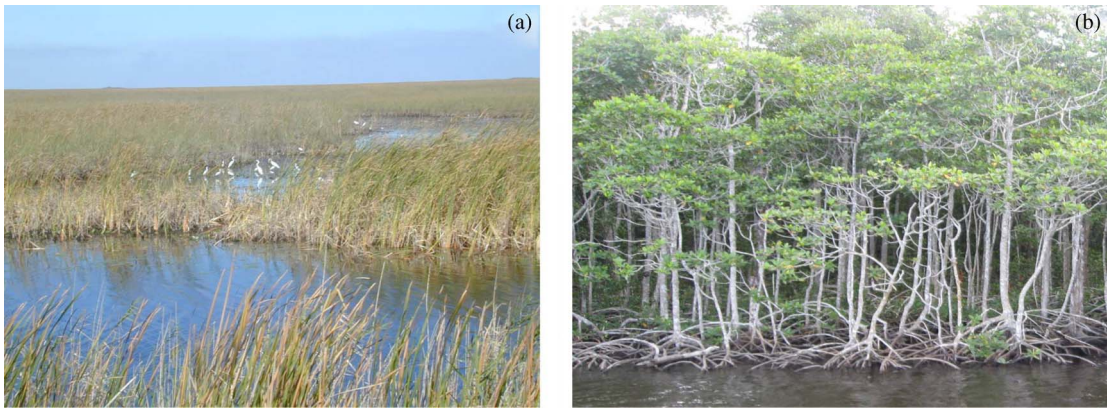

Fig. 2. Photograph images of (a) freshwater herbaceous vegetation (sawgrasses) and (b) saltwater woody vegetation (mangroves). The northeastern part of the study area consists of mostly freshwater herbaceous vegetation, whereas the southwestern area consists of mainly saltwater mangroves.

TABLE I
LIST OF RADARSAT-2 C-BAND SAR INTERFEROMETRIC PAIRS

Area	No	SAR image		$B_{\perp}$ [1]	B_{temp} [2]
		Master	Slave		
ENP [3]	1	2008-09-23	2008-10-17	414 m	24 days
ENP	2	2008-09-23	2008-11-10	88 m	48 days
ENP	3	2008-10-17	2008-11-10	502 m	24 days

[1] $B_{\perp}$ - absolute perpendicular baseline, [2] B_{temp} - temporal baseline,
[3] ENP – Everglades National Park (naturally flow wetlands).

different distributions of vegetation [Fig. 1(d)]. Previous TerraSAR-X (TSX) X-band InSAR studies reported an interesting change in fringe characteristic across the vegetation transition zone [24], [28], [29]. Fringes in the freshwater environment have long wavelength, reflecting slow water-level changes of the sheet flow, whereas the fringes in the saltwater environment are characterized by a short wavelength and a high fringe rate, reflecting rapid water-level changes due to ocean tides [24], [28], [29].

C. Data and Data Processing

RADARSAT-2 is a SAR satellite system operating with full quad-pol capability. The quad-pol data coverage is limited to a narrow swath (25 km) compared with other single or dual operating modes (50–100 km). This study is based on three acquisitions collected every 24-day repeat path over the study area between September 23, 2008, and November 10, 2008. The data were acquired in the fine-resolution quad-polarization (FQ6) beam mode with 5-m pixel resolution. The temporal baselines of the interferometric pairs are 24–48 days, and the geometric perpendicular baselines range from 88 to 502 m (Table I).

In this paper, we also use RADARSAT-2 quad-pol data that were acquired over the San Francisco area. We use this data set in order to demonstrate the power and importance of the new decomposition in splitting the cross-pol into both double-bounce and volume scattering components in urban environment. The San Francisco data were acquired with the fully polarimetric fine beam mode (FQ9) with 5-m pixel resolution and 25-km-wide swath. The data were provided as a promotional sample data set by the Canadian Space Agency.

TABLE II
RADARSAT-2 SAR DATA CHARACTERISTICS

Parameter	*Radarsat-2*	
	Everglades	*San Francisco*
Carrier frequency	5.405 GHz	
Wavelength	5.54 cm	
Polarization	Quad	
Repeat period	24 days	
Beam mode	Fine Quad (FQ6)	Fine Quad (FQ9)
Flight direction	Descending,	Ascending
Incidence angle	24.58 deg	28.02 deg
Pulse repetition frequency	2843.92 Hz	2763.52 Hz
ADC sampling rate	31.67 MHz	
Azimuth pixel spacing	4.70 m	4.82 m
Range pixel spacing	4.73 m	4.73 m

The characteristics of the RADARSAT-2 data sets used in this study are listed in Table II.

The Everglades data set was processed with the Repeat Orbit Interferometry PACkage (ROI_PAC) and GAMMA software to calculate phase changes between two acquisitions (interferograms) [30]. In all interferograms, we subtracted topographic-related phase changes calculated according to the SRTM-1 DEM and applied interferometric filtering to reduce the noise level [31]. PolSARpro was used to import data and to process the polarimetric decomposition [2].

D. InSAR Results

For each of the three interferometric pairs, we processed four (quad) interferograms, a separate interferogram for each polarization mode. Our results show very similar fringe pattern in all four quad interferograms representing water-level changes occurring between the acquisition times of each interferometric pair. These results confirm similar findings that we obtained in our previous studies of TSX dual-pol mode observations [24], [28], [29]. We present the co-pol interferograms as the sum and difference of the two co-pol phase changes (HH+VV and HH−VV) and the cross-pol (HV) interferogram as is in order to evaluate the effect on each scattering mechanism as suggested by the standard (Pauli) decomposition. The decomposition considers the following three scattering components: single bounce

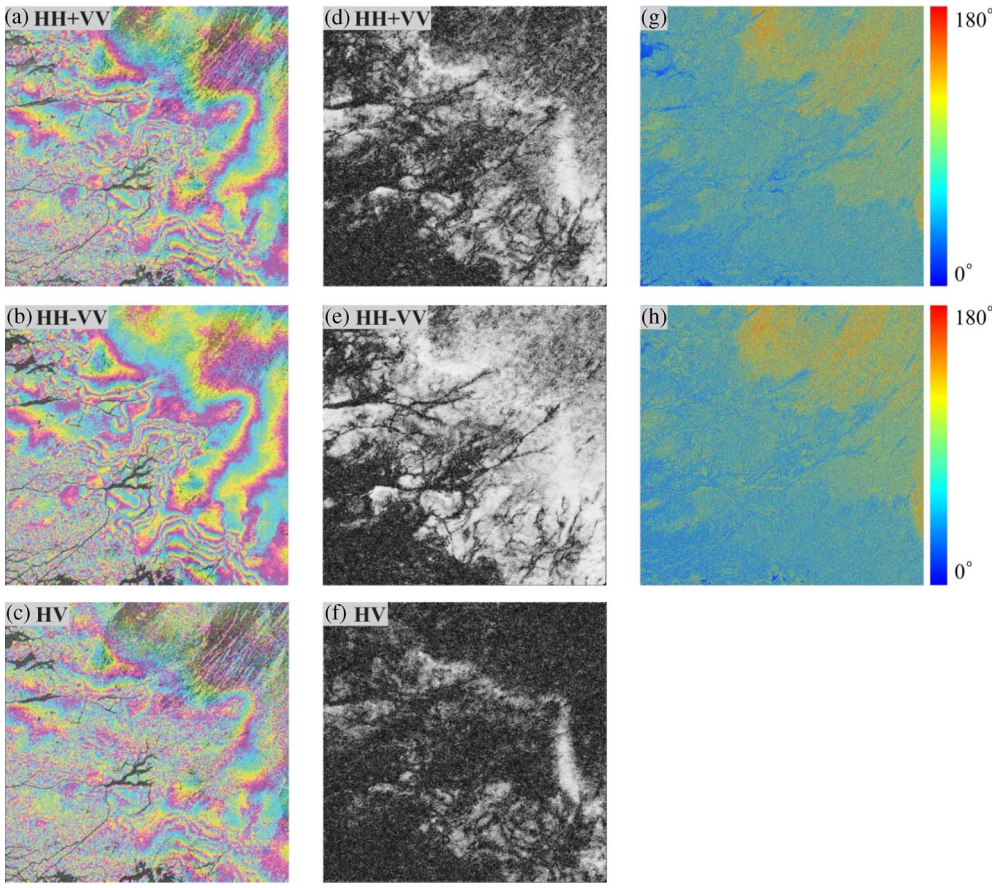

Fig. 3. Polarization interferograms and their coherence maps calculated according to standard scattering mechanism decomposition (Pauli). (a) and (d) Single bounce (HH+VV). (b) and (e) Double bounce (HH-VV). (c) and (f) Volume (HV). (g)–(h) Phase of the difference between HH and VV for each observation.

(HH+VV), double bounce (HH−VV), and volume scattering (HV or VH; Fig. 3). We present only the HV interferogram because the two cross-pol signals are assumed to be identical.

The interferograms show a low fringe rate in the northeastern corner, which is covered by herbaceous vegetated area. A high fringe rate along a wide-belt-oriented NW-SE is found in the central part of the interferogram in the low-height mangrove and shrub area. The phase is incoherent in the southwest corner, which is characterized by tall mangrove vegetation. These three zones correlate well with vegetation variations in this freshwater–saltwater transition zone.

The three polarization interferograms, which represent different scattering behavior, show a similar fringe pattern but different coherence levels. The coherence map of the HH−VV (double-bounce scattering) interferogram shows the highest values, and the second highest coherence is found in the HH+VV (single-bounce scattering) interferogram [Fig. 3(d) and (e)]. The HV (volume scattering) interferograms show the lowest coherence values [Fig. 3(f)]. Although the scattering phase centers of random targets cannot be derived explicitly from Pauli decomposition, the assumption that HV represents volume scattering is used by many decomposition studies [1], [3], [7], [8]. The coherence analysis confirms previous analyses, indicating that the double-bounce scattering is the dominant mechanism in wetland scattering [19], [24]. The region showing high coherence in Fig. 3(e) is in a good agreement with double-bounce dominant area, where the phase difference between HH and VV is around 180° for each observation in Fig. 3(g) and (h). However, note that the region of high coherence in cross-pol (HV) can be found only near the transition zone where moderate double-bounce scattering is found. In other words, it means that double-bounce scattering (high coherence) in the cross-pol cannot always be found in areas of dominant double-bounce scattering.

Interestingly or even surprisingly, the same fringe pattern reflecting water-level changes in both freshwater and saltwater wetlands was found in all three interferograms, including single bounce (HH+VV) and the cross-pol (HV). As wetland InSAR works due to the double-bounce scattering effect, we expected to find water-induced phase changes only in the double-bounce (HH−VV) interferograms. The occurrence of water-induced fringes in the single-bounce interferograms is somewhat surprising because, in the very flat water conditions of the Everglades (wind at water surface level is usually suppressed by vegetation), single bounce should scatter the radar pulse away from the satellite. Despite the very smooth water surface, single-bounce scattering can occur due to the smaller incidence angle because scattering at small incidence angles is sensitive enough to cause backscattering even from small perturbations in smooth surfaces. Alternatively, the unexpected single-bounce result can also be explained as a multiple odd scattering, which is part of the single-bounce formulation (HH+VV). Thus, the single-bounce interferogram most likely represents three or higher order odd bouncing of the electromagnetic wave,

including one from the water surface, which sampled the elevation change of the water surface.

The very surprising result is the occurrence of water-level change induced fringes in the cross-pol interferograms [HV; Fig. 3(c)]. This result cannot be explained by volume scattering, as assumed by most vegetation scattering theories, because the upper levels of the vegetation, which move easily by wind, are not stable scatterers for spaceborne repeat pass interferometry. Thus, we suggest that the cross-pol signal contains a multipath component, which also bounces off the water surface and samples the changing water levels. The simplest scattering mechanism for cross-pol multiple path is a rotated dihedral. A regular dihedral, where the scattering surfaces are horizontal (water) and vertical (vegetation), keeps the same polarization throughout the radar scattering path. However, when one of the scattering surfaces is tilted (e.g., slanted vegetation), the scattering off the tilted surface results in a multiple interaction of the polarized electromagnetic signal. Consequently, some of the scattered signal changes its polarization. The slanted root structure of mangroves [Fig. 2(b)] can serve as a good example for the suggested rotated dihedral model. However, low coherence maps indicate that tilted dipole structures in the freshwater herbaceous vegetated wetland [Fig. 2(a)] might not be a good source for maintaining the coherence in the cross-pol interferogram.

Although the proposed rotated dihedral mechanism was derived from phase observations, it also applies to amplitude observations. Therefore, we suggest that the cross-pol amplitude signal can be decomposed into two components: one accounting for the "traditional" volume scattering and the other for the newly defined cross-pol ground scattering due to rotated dihedrals.

III. Polarimetric Decomposition

Here, we present a modified decomposition approach, which considers the occurrence of a rotated dihedral plane. The decomposition follows the polarimetric compensation proposed by Yamaguchi *et al.* [9], [10]. The scattering matrix is written for simplicity, assuming $S_{\mathrm{HV}} = S_{\mathrm{VH}}$:

$$[S(\mathrm{HV})] = \begin{bmatrix} S_{\mathrm{HH}} & S_{\mathrm{HV}} \\ S_{\mathrm{VH}} & S_{\mathrm{VV}} \end{bmatrix} = \begin{bmatrix} a & c \\ c & b \end{bmatrix}. \tag{1}$$

We utilize a 3×3 coherency matrix calculated in the Pauli matrix basis to derive each component mathematically as in (2), shown at the bottom of the page, following the scheme provided by Yamaguchi *et al.* [8]. In (2), $\langle\ \rangle$ denotes the ensemble average of a few pixels in the data processing, and $*$ denotes a complex conjugate.

The measured coherency matrix can be divided into four submatrices as follows:

$$\begin{aligned} \langle |T| \rangle^{\mathrm{HV}} &= \begin{bmatrix} T_{11} & T_{12} & T_{13} \\ T_{21} & T_{22} & T_{23} \\ T_{31} & T_{32} & T_{33} \end{bmatrix} \\ &= f_s [T]^{\mathrm{hv}}_{\mathrm{single}} + f_d [T]^{\mathrm{hv}}_{\mathrm{double}} + f_v [T]^{\mathrm{hv}}_{\mathrm{volume}} \\ &\quad + f_{rd} [T]^{\mathrm{hv}}_{\mathrm{rotated\_diplane}} \end{aligned} \tag{3}$$

where f_s, f_d, f_v, and f_{rd} are the coefficients related to the powers of the single-bounce, double-bounce from co-pol, volume, and double-bounce scattering components from cross-pol, respectively. Also, $\langle |T| \rangle^{\mathrm{HV}}$ is the term of spatial ensemble averaging of the actually measured data, while $\langle |T| \rangle^{\mathrm{hv}}$ results from mathematical averaging formulation like in [8].

As proposed in the Yamaguchi's four-component method [8], we adopted the scattering coherency matrix in the single, double, and volume scattering as follows:

$$\begin{aligned} \langle |T| \rangle^{\mathrm{hv}}_{\mathrm{single}} &= \begin{bmatrix} 1 & \beta^* & 0 \\ \beta & |\beta|^2 & 0 \\ 0 & 0 & 0 \end{bmatrix} \\ \langle |T| \rangle^{\mathrm{hv}}_{\mathrm{double}} &= \begin{bmatrix} |\alpha|^2 & \alpha & 0 \\ \alpha^* & 1 & 0 \\ 0 & 0 & 0 \end{bmatrix} \\ \langle |T| \rangle^{\mathrm{hv}}_{\mathrm{volume}} &= \frac{1}{4} \begin{bmatrix} 2 & 0 & 0 \\ 0 & 1 & 0 \\ 0 & 0 & 1 \end{bmatrix}. \end{aligned} \tag{4}$$

The coherency matrix is derived from the mathematical form of averaging with respect to the probability density function $p(\theta)$[8] as follows:

$$\langle S_{\mathrm{hv}} S^*_{\mathrm{hv}} \rangle = \int_0^{2\pi} S_{\mathrm{hv}} S^*_{\mathrm{hv}} p(\theta) d\theta. \tag{5}$$

Assuming that the probability density function is uniform $[p(\theta) = 1/(2\pi)]$, the mathematical averaging of the coherency matrix can be integrated as shown by Yamaguchi *et al.* [7], [8] and is presented here

$$\begin{aligned} &\langle |T| \rangle^{\mathrm{hv}} \\ &= \begin{bmatrix} \frac{1}{2}|a+b|^2 & 0 & 0 \\ 0 & \frac{1}{4}|a-b|^2 + |c|^2 & +j\mathrm{Im}\{c^*(a-b)\} \\ 0 & -j\mathrm{Im}\{c^*(a-b)\} & \frac{1}{4}|a-b|^2 + |c|^2 \end{bmatrix}. \end{aligned} \tag{6}$$

$$\langle |T| \rangle^{\mathrm{HV}} = \begin{bmatrix} \frac{1}{2}\left\langle |S_{\mathrm{HH}} + S_{\mathrm{VV}}|^2 \right\rangle & \frac{1}{2}\left\langle (S_{\mathrm{HH}} + S_{\mathrm{VV}})(S_{\mathrm{HH}} - S_{\mathrm{VV}})^* \right\rangle & \left\langle (S_{\mathrm{HH}} + S_{\mathrm{VV}}) S^*_{\mathrm{HV}} \right\rangle \\ \frac{1}{2}\left\langle (S_{\mathrm{HH}} - S_{\mathrm{VV}})(S_{\mathrm{HH}} + S_{\mathrm{VV}})^* \right\rangle & \frac{1}{2}\left\langle |S_{\mathrm{HH}} - S_{\mathrm{VV}}|^2 \right\rangle & \left\langle (S_{\mathrm{HH}} - S_{\mathrm{VV}}) S^*_{\mathrm{HV}} \right\rangle \\ \left\langle S_{\mathrm{HV}} (S_{\mathrm{HH}} + S_{\mathrm{VV}})^* \right\rangle & \left\langle S_{\mathrm{HV}} (S_{\mathrm{HH}} - S_{\mathrm{VV}})^* \right\rangle & \left\langle 2|S_{\mathrm{HV}}|^2 \right\rangle \end{bmatrix} \tag{2}$$

Although the cosine squared distribution in the selection of probability density distribution function is usually used for vertical structures, we adhere to apply uniform distribution from empirical experiment over two study areas. The power of cross-pol double-bounce scattering with both cosine squared distribution and uniform distribution shows almost similar features in the natural environment of Everglades wetland. However, loss of power in cross-pol double-bounce scattering is detected with cosine squared distribution in man-made building structure environment of the San Francisco study area. Thus, we take a randomly distributed model with dihedral plane using (6) for the double-bounce scattering model in the cross-pol signal. The scattering coherency matrix for rotated diplane is

$$[S]^{\mathrm{HV}} = \begin{bmatrix} 1 & 0 \\ 0 & -1 \end{bmatrix} \text{ or } [S]^{\mathrm{HV}} = \begin{bmatrix} -1 & 0 \\ 0 & 1 \end{bmatrix}$$

$$\Rightarrow \langle |T| \rangle^{\mathrm{hv}}_{\mathrm{rotated\_diplane}} = \frac{1}{2} \begin{bmatrix} 0 & 0 & 0 \\ 0 & 1 & 0 \\ 0 & 0 & 1 \end{bmatrix}. \quad (7)$$

From (7), we can estimate the cross-pol double-bounce component. The coherency matrix in (3) can now be written as a combination of single-bounce, double-bounce from co- and cross-pol, and volume scattering component as follows:

$$\begin{aligned} \langle |T| \rangle^{\mathrm{HV}} &= f_s [T]^{\mathrm{hv}}_{\mathrm{single}} + f_d [T]^{\mathrm{hv}}_{\mathrm{double}} \\ &\quad + f_v [T]^{\mathrm{hv}}_{\mathrm{volume}} + f_{rd} [T]^{\mathrm{hv}}_{\mathrm{rotated\_diplane}} \\ &= f_s \begin{bmatrix} 1 & \beta^* & 0 \\ \beta & |\beta|^2 & 0 \\ 0 & 0 & 0 \end{bmatrix} + f_d \begin{bmatrix} |\alpha|^2 & \alpha & 0 \\ \alpha^* & 1 & 0 \\ 0 & 0 & 0 \end{bmatrix} \\ &\quad + \frac{f_v}{4} \begin{bmatrix} 2 & 0 & 0 \\ 0 & 1 & 0 \\ 0 & 0 & 1 \end{bmatrix} + \frac{f_{rd}}{2} \begin{bmatrix} 0 & 0 & 0 \\ 0 & 1 & 0 \\ 0 & 0 & 1 \end{bmatrix}. \quad (8) \end{aligned}$$

Comparing each coefficient (f_s, f_d, f_v, and f_{rd}) with the coherency matrix elements using (8) yields four equations with six unknown parameters as follows:

$$\begin{aligned} &\frac{1}{2} \left\langle |S_{\mathrm{HH}} + S_{\mathrm{VV}}|^2 \right\rangle = f_s + f_d |\alpha|^2 + \frac{f_v}{2} \\ &\frac{1}{2} \left\langle |S_{\mathrm{HH}} - S_{\mathrm{VV}}|^2 \right\rangle = f_s |\beta|^2 + f_d + \frac{f_v}{4} + \frac{f_{rd}}{2} \\ &2 \left\langle |S_{\mathrm{HV}}|^2 \right\rangle = \frac{f_v}{4} + \frac{f_{rd}}{2} \\ &\frac{1}{2} \left\langle (S_{\mathrm{HH}} + S_{\mathrm{VV}})(S_{\mathrm{HH}} - S_{\mathrm{VV}})^* \right\rangle = f_s \beta^* + f_d \alpha. \quad (9) \end{aligned}$$

However, the aforementioned four equations are underdetermined because there are six unknown parameters (f_s, f_d, f_v, f_{rd}, α, and β). In order to solve the equations, we need to make additional assumptions and fix the values of two of the unknown parameters. Following Yamaguchi *et al.* [8], in each scattering environment, we fix two different parameters. In a high cross-pol environment, we assume that the surface scattering is negligible ($f_s = 0$), which simplify the equations as follows:

$$\begin{aligned} &\frac{1}{2} \left\langle |S_{\mathrm{HH}} + S_{\mathrm{VV}}|^2 \right\rangle = f_d |\alpha|^2 + \frac{f_v}{2} \\ &\frac{1}{2} \left\langle |S_{\mathrm{HH}} - S_{\mathrm{VV}}|^2 \right\rangle = f_d + \frac{f_v}{4} + \frac{f_{rd}}{2} \\ &2 \left\langle |S_{\mathrm{HV}}|^2 \right\rangle = \frac{f_v}{4} + \frac{f_{rd}}{2} \\ &\frac{1}{2} \left\langle (S_{\mathrm{HH}} + S_{\mathrm{VV}})(S_{\mathrm{HH}} - S_{\mathrm{VV}})^* \right\rangle = f_d \alpha. \quad (10) \end{aligned}$$

Now, the four unknowns can be estimated by reorganizing the equations

$$\begin{aligned} f_d &= \frac{1}{2} \left\langle |S_{\mathrm{HH}} - S_{\mathrm{VV}}|^2 \right\rangle - 2 \left\langle |S_{\mathrm{HV}}|^2 \right\rangle \\ \alpha &= \frac{\langle (S_{\mathrm{HH}} + S_{\mathrm{VV}})(S_{\mathrm{HH}} - S_{\mathrm{VV}})^* \rangle}{2 f_d} \\ f_v &= 2 \cdot \left(\frac{1}{2} \left\langle |S_{\mathrm{HH}} + S_{\mathrm{VV}}|^2 \right\rangle - f_d |\alpha|^2 \right) \\ f_{rd} &= 2 \cdot \left(2 \left\langle |S_{\mathrm{HV}}|^2 \right\rangle - \frac{f_v}{4} \right). \quad (11) \end{aligned}$$

Thus, we can determine the scattering powers of P_d, P_{rd}, and P_v as follows:

$$P_{rd} > 0: \quad P_d = f_d \left(1 + |\alpha|^2\right),\ P_v = f_v,\ P_{rd} = f_{rd}. \quad (12)$$

However, whenever the solution of (11) results in $f_{rd} \leq 0$, the assumption of a high cross-pol environment is not consistent with the observation. A negative or zero value of f_{rd} defines our low cross-pol scattering scenario. We now set $P_{rd} = f_{rd} = 0$ and follow the same decomposition procedure of Yamaguchi's four-component decomposition approach [8] ignoring helix component. According to their formulations, in area of high surface scattering ($\mathrm{Re}\langle S_{\mathrm{hh}} S_{\mathrm{vv}} \rangle > 0$), double bounce is neglected ($\alpha = 0$), whereas in areas of low surface scattering ($\mathrm{Re}\langle S_{\mathrm{hh}} S_{\mathrm{vv}} \rangle < 0$), surface scattering is neglected ($\beta^* = 0$) to estimate unknown parameters in (13) and (14), which is derived by Yamaguchi *et al.* [8]. The derived equations of their formulation are provided in Fig. 4, which present a flowchart of our decomposition algorithm. The decomposition formulations provide quantitative estimates for cross-pol double-bounce and other scattering components, based on the coherency matrix

$$\begin{aligned} &\mathrm{Re}\langle S_{\mathrm{hh}} S_{\mathrm{vv}} \rangle > 0 \\ &f_v = 8 \left\langle |S_{\mathrm{HV}}|^2 \right\rangle \\ &f_s = \frac{1}{2} \left\langle |S_{\mathrm{HH}} + S_{\mathrm{VV}}|^2 \right\rangle - 4 \left\langle |S_{\mathrm{HV}}|^2 \right\rangle \\ &\beta^* = \frac{\langle (S_{\mathrm{HH}} + S_{\mathrm{VV}})(S_{\mathrm{HH}} - S_{\mathrm{VV}})^* \rangle}{2 f_s} \\ &f_d = \frac{1}{2} \left\langle |S_{\mathrm{HH}} - S_{\mathrm{VV}}|^2 \right\rangle - 2 \left\langle |S_{\mathrm{HV}}|^2 \right\rangle \\ &\qquad - \frac{1}{2} \beta^* \left\langle (S_{\mathrm{HH}} + S_{\mathrm{VV}})(S_{\mathrm{HH}} - S_{\mathrm{VV}})^* \right\rangle \quad (13) \end{aligned}$$

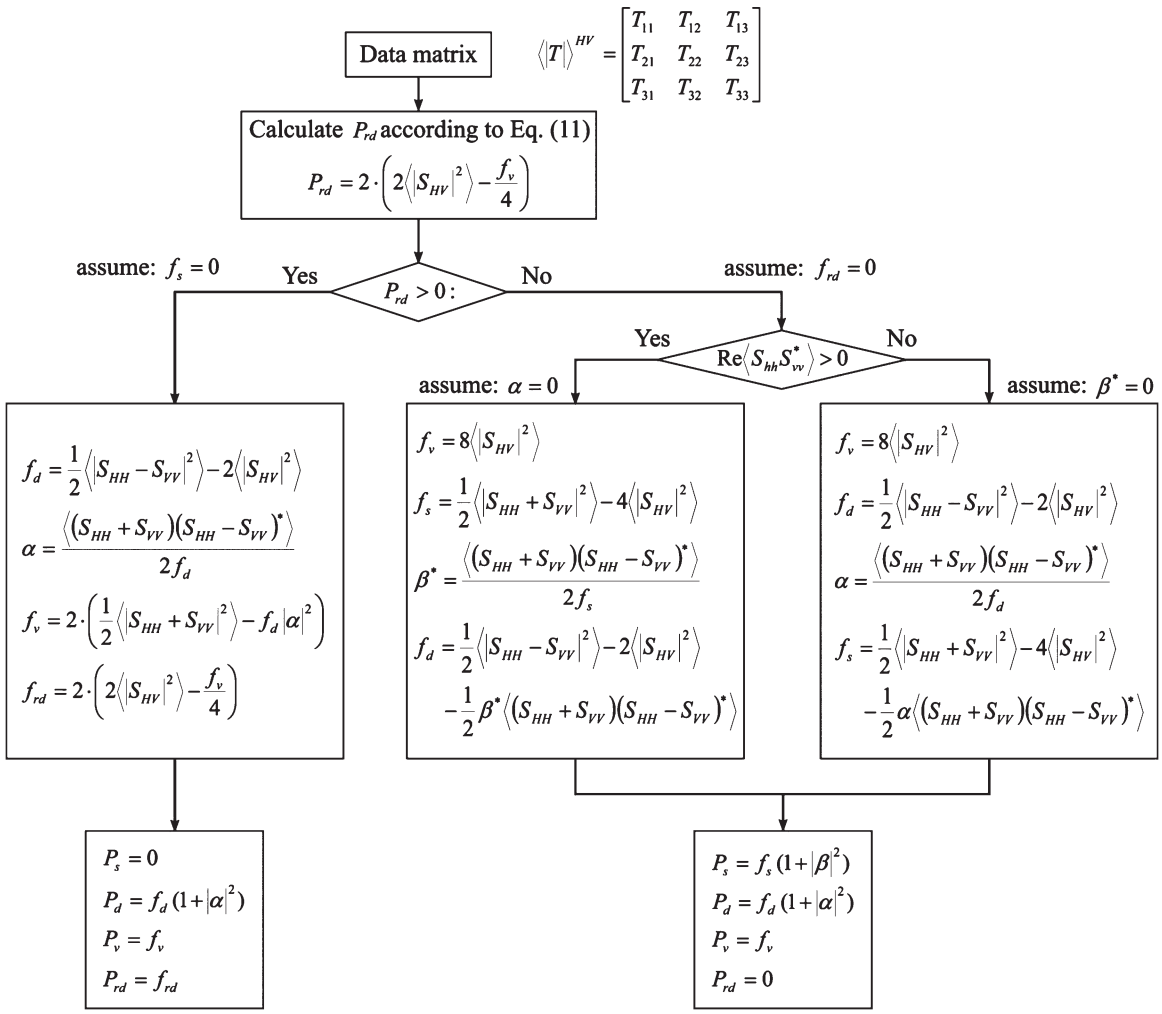

Fig. 4. Four-component power decomposition algorithm with surface (P_s), co-pol double-bounce (P_d), volume (P_v), and cross-pol double-bounce (P_{rd}) scattering mechanisms.

$$
\begin{aligned}
&\mathrm{Re}\langle S_{\mathrm{hh}} S_{\mathrm{vv}} \rangle < 0 \\
&f_v = 8 \langle |S_{\mathrm{HV}}|^2 \rangle \\
&f_d = \frac{1}{2} \langle |S_{\mathrm{HH}} - S_{\mathrm{VV}}|^2 \rangle - 2 \langle |S_{\mathrm{HV}}|^2 \rangle \\
&\alpha = \frac{\langle (S_{\mathrm{HH}} + S_{\mathrm{VV}})(S_{\mathrm{HH}} - S_{\mathrm{VV}})^* \rangle}{2 f_d} \\
&f_s = \frac{1}{2} \langle |S_{\mathrm{HH}} + S_{\mathrm{VV}}|^2 \rangle - 4 \langle |S_{\mathrm{HV}}|^2 \rangle \\
&\qquad - \frac{1}{2} \alpha \langle (S_{\mathrm{HH}} + S_{\mathrm{VV}})(S_{\mathrm{HH}} - S_{\mathrm{VV}})^* \rangle .
\end{aligned} \tag{14}
$$

Thus, we can determine the scattering powers of P_s, P_d, and P_v as follows:

$$
P_{rd} \leq 0 : \quad P_s = f_s \left(1 + |\beta|^2 \right), P_d = f_d \left(1 + |\alpha|^2 \right), P_v = f_v . \tag{15}
$$

Here, we can obtain a quantitative estimate for cross-pol double-bounce scattering component based on the coherency matrix. A flowchart of the decomposition algorithm is shown in Fig. 4.

IV. Results

A. San Francisco Urban Environment Study

We first applied our new decomposition method to the urban environment of the San Francisco area using the RADARSAT-2 promotional sample data set. This part of our study demonstrates the strength of our decomposition by comparing its results to various decomposition approaches that have been tested [2]. Using our new decomposition method, we calculated the following four scattering components: single bounce, double bounce from co- and cross-pol, and volume scattering [Fig. 5(a)–(d)]. The performance of our decomposition method shows typical features of each scattering behavior in overall area compared with the previous decomposition approaches [2].

Based on our four-component decomposition, we generated a color composite image showing the dominant scattering mechanism in each area [Fig. 5(e)]. In this image, the double-bounce component (P_d—red) contains contribution from both the co- and cross-pol observations [Fig. 5(b) and (c)], whereas the single-bounce (P_s—blue) and volume scattering (P_v—green) components are presented as calculated by the decomposition [Fig. 5(a) and (d)], respectively. The color composite map shows that the scattering is dominated by single bounce (blue)

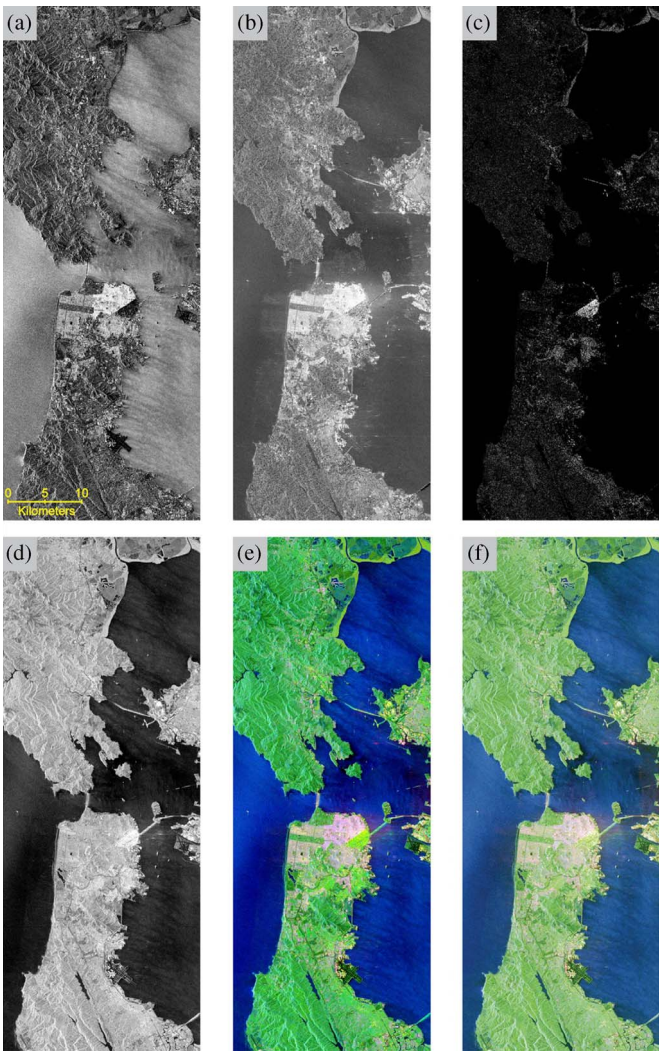

Fig. 5. Proof-of-concept study showing decomposition analysis of RADARSAT-2 data set acquired over the San Francisco area. (a) Single-bounce component. (b) Double-bounce component from co-pol. (c) Double-bounce component from cross-pol. (d) Volume scattering component. (e) Decomposition color composite image using our approach: blue—single bounce, red—double bounce (both from co- and cross-pol), and green—volume scattering. (f) Decomposition color composite image using Yamaguchi's method based on polarimetric orientation compensation.

in the ocean, by double bounce (red) in the urban area, and by volume scattering (green) in open vegetated areas. It is important to notice that some of the double bounce in the urban area arises from the cross-pol component.

In order to validate the performance of our decomposition, we compared our results with those from the four-component decomposition of Yamaguchi *et al.* [9], which accounts polarimetric orientation compensation (Figs. 5 and 6). Overall, our decomposition results show a good agreement with Yamaguchi's four polarimetric decompositions [Fig. 5(e) and (f)]. To see more details, we zoomed in the urban area of San Francisco (Fig. 6). The comparison shows that Yamaguchi's [8] previous decomposition without polarimetric orientation compensation [Fig. 6(a)] yields stronger volume scattering component power compared with the decomposition results with polarimetric orientation compensation [Fig. 6(b)], especially in the urban area with diagonally oriented street directions.

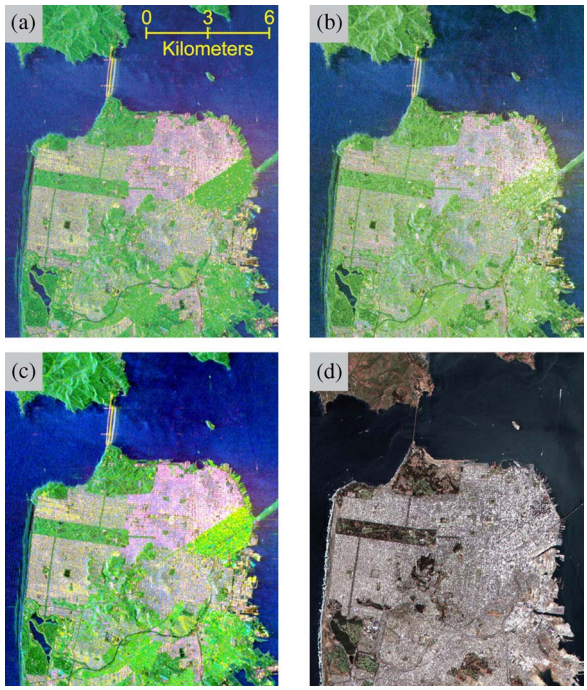

Fig. 6. Zoomed images of decomposition results. (a) Yamaguchi's four-component approach. (b) Yamaguchi's four-component approached with polarimetric orientation compensation. (c) Decomposition color composite image of our approach: blue—single bounce, red—double bounce (both from co- and cross-pol), and green—volume scattering. (d) Landsat-7 ETM+ optic color composite image (http://www.landcover.org/data/landsat/).

Our decomposition result [Fig. 6(c)] shows similar features as Yamaguchi's decomposition result with polarimetric orientation compensation and generates a more distinct color composite image with better contrast in overall. A good correspondence between open areas (especially the Golden Gate Park) can be detected by comparing our color composite map [Fig. 6(c)] with the optical color composite image of Landsat-7 ETM+ [http://www.landcover.org/data/landsat; Fig. 6(d)].

In order to evaluate the relations between the co- and cross-pol double-bounce components, we zoomed in the urban area of San Francisco (Fig. 7). Two components of the cross-pol double bounce [Fig. 7(b)] and volume scattering [Fig. 7(c)] can be separated from the cross-pol (HV) data [Fig. 7(a)]. The advantage of our decomposition lies in its capability to extract the cross-pol double-bounce scattering component, which was ignored by previous decomposition methods. Thus, we can also get the double-bounce component in the cross-pol. The cross-pol double bounce can be found clearly in urban area with differently oriented street directions and at the Golden Gate Bridge. Consequently, the double-bounce component has increased due to the addition of the cross-pol double bounce [Fig. 7(d)], whereas the volume scattering component has decreased [Fig. 7(c)].

We compare the contribution of the co- and cross-pol double-bounce components in different urban environments by displaying a color composite image of both components [Fig. 8(a)]. The double-bounce scattering from the co-pol (red) is dominant at the yellow circle area, where the street orientation (N-S) is almost orthogonal to the radar direction of illumination. Double-bounce scattering from the cross-pol (green) can be

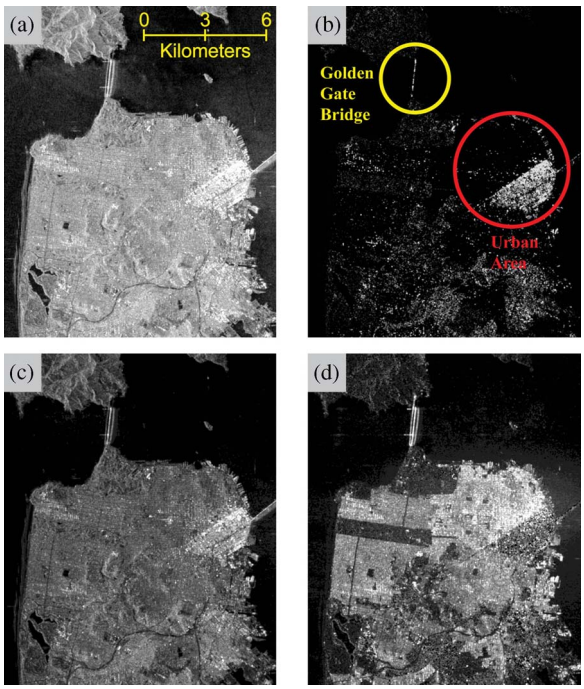

Fig. 7. Zoomed images of the decomposition results. (a) Cross-pol (HV). (b) Cross-pol double-bounce component. (c) Volume scattering component. (d) Both co- and cross-pol double-bounce components.

detected at the red circle, where the street orientation (NE-SW) is roughly diagonal to the radar direction of illumination. The cross-pol double-bounce scattering is detected in vegetated area and urban area of diagonal structures which are volume scattering dominant area, whereas the co-pol double-bounce scattering is dominant over typical urban area.

In order to validate our decomposition results, power values of each component are displayed as profiles along the lines B-B′ and C-C′ [Fig. 8(b)–(d)]. The profile across the urban area (B-B′) shows that the co-pol double-bounce component (red line) in the area with N-S oriented streets is stronger than in the area of diagonal streets [Fig. 8(b)]. The level of cross-pol double bounce in the diagonal streets area is stronger than co-pol scattering; hence, the total double-bounce component has increased due to a contribution from cross-pol double-bounce scattering. Profiles of single, double, and volume scattering components calculated by our and Yamaguchi's decompositions with polarimetric orientation compensation are displayed in Fig. 8(c). A comparison between the two decompositions shows very little differences in both single and double-bounce scattering components in overall. However, the profile of the volume scattering component [green line in Fig. 8(c)] indicates that our decomposition results show slightly large power because the volume scattering component of Yamaguchi's approach was minimized by polarimetric orientation compensation.

We also evaluated the results of our decomposition along a profile orthogonal to the Golden Gate Bridge [Fig. 8(d)], which shows the classic triple bouncing off the bridge [32], [33]. The background scattering is dominated by single bounce off the ocean surface. The first bounce (first peak to the left), which is often called single bounce [32], cannot be detected from the single-bounce component (blue line) but rather from the double-bounce component (purple), suggesting that the first bounce occurs due to co-pol double-bounce scattering off the bridge structures (horizontal road and vertical metal pipes). The second peak, which is the dominate one, occurs mainly due to co-pol double bounce, as the signal scatters twice, once from the bridge and the other from the water surface, or vice versa. The third bounce, known as triple bounce, shows medium scattering of both co-pol components, single and double bounce, and also some volume scattering. The single-bounce component, which includes all odd scattering, is a combination of background single-bounce and additional triple-bounce components. The double and volume scattering components in the triple bounce suggest a more complex scattering of the bridge and water surfaces than previously considered [32].

The double-bounce component from the cross-pol is calculated from T_{33}, and the helix component is estimated with the co- and cross-pol correlations from the imaginary part of T_{23}. The helix component is well identified in urban areas but basically disappears in natural distributed scatterer environment [34], whereas the cross-pol double-bounce scattering component can be estimated in both urban area and natural distributed scatterer environments.

B. *Everglades Wetland Study*

We now apply our decomposition approach to the RADARSAT-2 data set acquired over the Everglades wetlands in order to evaluate its quality in rural environments. We decomposed the cross-pol amplitude [HV; Fig. 9(a)] into double-bounce scattering and volume scattering. In order to discriminate the double-bounce effect in the cross-pol, we displayed the color composite image with the double-bounce component in red and volume scattering in green [Fig. 9(b)]. The power of cross-pol double-bounce scattering was detected over mangrove vegetated area in the transition zone between freshwater and saltwater ecosystems supporting the new model, which considers the slanted root structure of the saltwater mangroves as good source of rotated diplane scatterers. Although the coherence maps are enhanced by interferometric phase filtering, an overall low coherence value of the cross-pol is estimated. In order to verify the decomposition results, we displayed both the interferometric coherence (light green) and the cross-pol double-bounce scattering component (red), as shown in Fig. 10. Most of the high-coherence areas can be found in the transition zone between freshwater and saltwater ecosystems, where the cross-pol double scattering component is dominant. This zone is characterized by a mixture of vegetation type, including short and intermediate high mangroves. The area with tall mangrove is located in the southwest corner of the image and is characterized by volume scattering (dark green). In this area, the radar signal interacts mainly with the upper sections of the vegetation and does not sample the water surface beneath the vegetation. Since the cross-pol signal can be severely affected by temporal decorrelation especially in wetland InSAR application, we cannot compare directly the double-bounce component with coherence [Fig. 3(f)] in the cross-pol. The coherence in the freshwater herbaceous vegetation is much lower than in the saltwater mangrove forest.

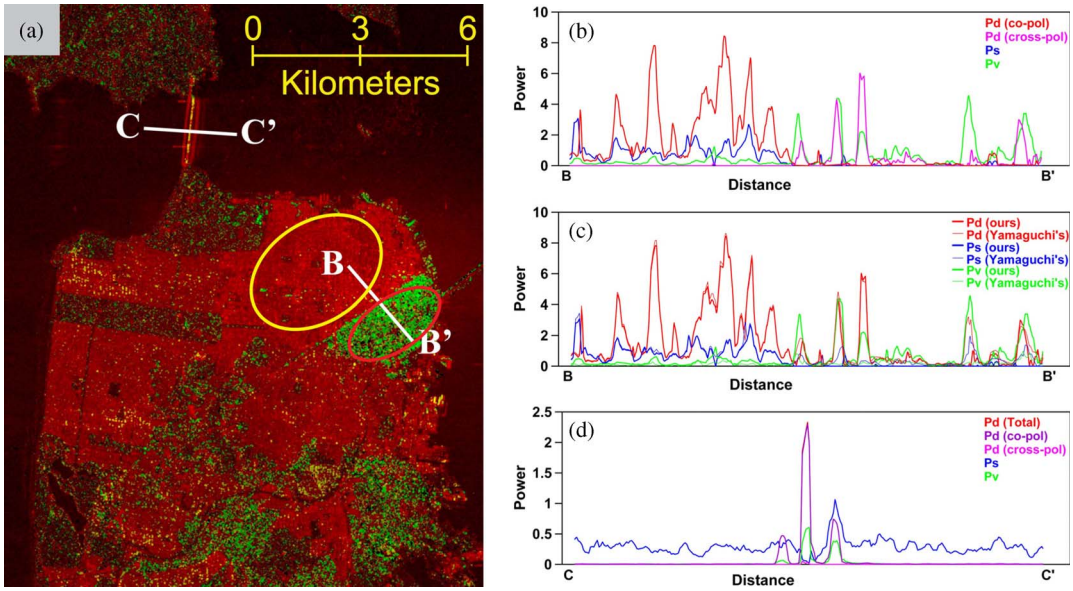

Fig. 8. (a) Color composite image of co-pol (red) and cross-pol (green) double-bounce components. (b) and (c) Profile in the urban area (B-B′) showing power variations of each scattering component due to variation in street orientation. Higher values in the left-hand side occur where streets are aligned normal to the radar illumination direction, whereas lower values on the right-hand-side occur where streets are oriented diagonally to the radar illumination direction. (d) Power profile of C-C′ across the Golden Gate Bridge.

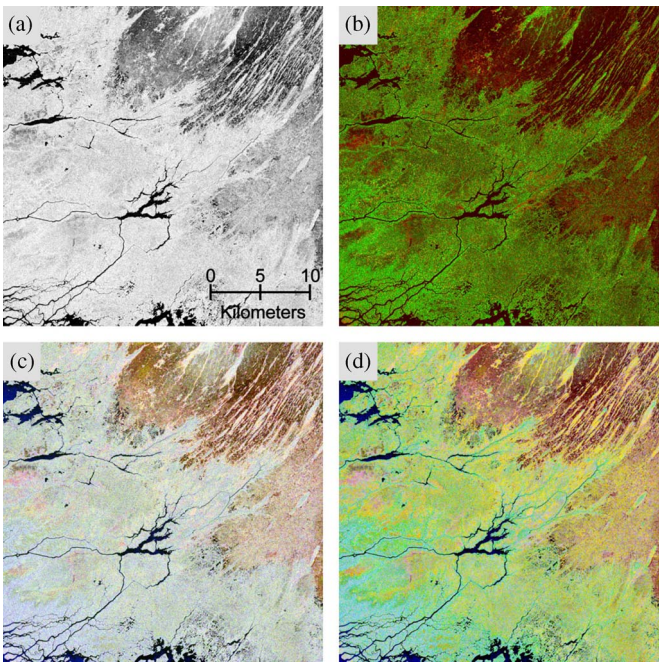

Fig. 9. SAR amplitude and decomposition results of the Everglades study area (location in Fig. 1). (a) Cross-pol (HV) amplitude image. (b) Color composite map with the cross-pol double-bounce (red) and volume scattering (green) components in the cross-pol signal. (c) Color composite image using Yamaguchi's four decomposition. (d) Color composite image using our decomposition approach: single bounce (blue), double bounce (red), and volume scattering (green).

We attribute the higher coherence in the saltwater wetland to thicker woody mangrove vegetation in the mangrove forest environment. In Figs. 3 and 9(b), the fringes of the cross-pol interferograms can be detected in the region where double-bounce scattering is dominant in the cross-pol. Moreover, the double-bounce dominant area in the cross-pol is closely related

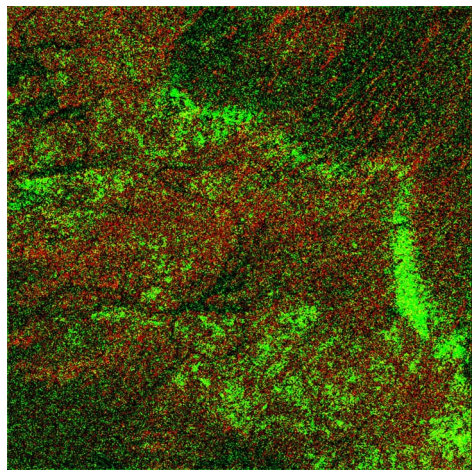

Fig. 10. Color composite image with the cross-pol double-bounce scattering component (red) overlain by interferometric coherence (light green).

to coherence of interferogram with HH-VV signal [Fig. 3(e)]. This implies that both double-bounce components in the co- and cross-pol can be scattered from similar surface's target.

The decomposed color composite images from our approach and Yamaguchi's four-component decomposition with polarimetric orientation compensation are displayed with double bounce (P_d) in red, single bounce (P_s) in blue, and volume scattering (P_v) in green [Fig. 9(c) and (d)]. The simplest decomposition using the Pauli scattering matrix can provide a color composite map to understand the scattering mechanism [Fig. 1(c)]. We notice that three color composite maps [Pauli, Fig. 1(c); Yamaguchi, Fig. 9(c); and ours, Fig. 9(d)] show similar features to indicate the overall scattering mechanism. However, we can notice that more dominant double-bounce scattering components can be found in the freshwater herbaceous area and transition zone between the freshwater and

saltwater areas which show coherent interferometric phases of water-level changes. The dominant double-bounce scattering areas can be clearly detected through the color composite image, which cannot be represented by previous decomposition approaches, displayed with the double-bounce component in red and volume scattering in green [Fig. 9(b)].

We notice three following characterized areas: 1) double-bounce scattering dominant in the freshwater herbaceous northeastern area; 2) volume scattering dominant area in the saltwater mangrove area; and 3) dominant surface scattering from the aquatic surface and tall dense vegetated southwestern area. These characteristics are well correlated with the Landsat-7 ETM+ optic color composite image in Fig. 1(d) and the InSAR results described in Section II-D.

V. Discussion

Multiple polarimetric SAR amplitude observations have been widely used to estimate vegetation scattering using various target decompositions [2], [3], [6]–[8], [13]–[17]. In most of the decomposition algorithms, the cross-pol has been assumed to represent solely volume scattering in vegetated area. This assumption has been used mainly to keep the orthogonality of the scattering mechanism. However, wetland InSAR phase information [Fig. 3(c)] indicates that the cross-pol signal samples the water surface beneath the vegetation, suggesting that the cross-pol signal does not represent solely volume scattering. We proposed that the cross-pol signal contains also a double-bounce component arising from the interaction of the radar signal with slanted vegetation that can be modeled as rotated dihedrals. In dense vegetation, however, the double-bounce component vanishes, and the cross-pol signal is dominated by volume scattering, as observed in the tall mangrove forest located in the southwestern corner of the Everglades study area [Fig. 3(b)]. In this area, the radar signal cannot penetrate into the ground due to the tall and dense vegetation, resulting in an incoherent phase signal, which reflects volume scattering in the upper sections of the vegetation. Although the proposed model assumes a randomly oriented root structure, which serves as diplanes for the bistatic specular scattering, not all the roots act as diplanes. For any given acquisition geometry, only a small number of roots that are correctly oriented with respect to the satellite serve as diplanes and enable the cross-pol double-bounce scattering.

The limitation of previous decomposition algorithms has been raised in recent publications [9], [10], [13]. For example, van Zyl *et al.* [13] pointed out that the volume scattering has been overestimated in previous model-based decomposition algorithms. They suggested that the cross-pol signal might come from the underlying ground surface. In other studies, Yamaguchi *et al.* and Lee and Ainsworth [9], [10] explained that the observed excessive volume scattering is affected by the polarization orientation angle. They modeled this effect by the rotation of coherency matrix, which reduced the volume scattering power and increased the power of double-bounce scattering component. The results of their studies are consistent with our observation that some portion of the cross-pol signal reflects double-bounce scattering.

All of the recent decomposition approaches [9], [10], [13] including our study point out that the volume scattering is overestimated in previous model-based decomposition algorithms and it can contain a portion of underlying ground surface scattering. In order to decrease power of the volume scattering component, Yamaguchi *et al.* [9] and Lee and Ainsworth [10] proposed the orientation angle compensation by multiplying the rotation matrix to the coherency matrix. van Zyl *et al.* [13] suggested a nonnegative eigenvalue decomposition approach, which compensates the overestimated volume scattering component by a simple addition of the remainder matrix to the existing scattering models. Although the aforementioned two decomposition approaches have reduced the volume scattering component and increased the power of the double-bounce scattering component, they do not suggest a decomposition of double-bounce component from the cross-pol signal. Our approach adopts the rotated dihedral model and enables us to extract the cross-pol double-bounce component.

The extraction of inherent volume scattering component can be important for the ground biomass estimate studies. Insofar, these studies compare ground-based estimates with typical HV, which typically shows a large range of values. Our study suggests that only a portion of the HV signal reflects volume scattering and the rest of the underlying ground surface scattering. The biomass estimation should not be based strictly on the volume scattering power. However, we expect to find a better comparison with ground-based studies when comparing it to the volume scattering component calculated by our decomposition, which removes the double bounce from the cross-pol signal.

Our decomposition algorithm performed well in both urban and rural environments but still has its limitations. The two main problems that limit the algorithm are the negative power that is found in some pixels and the domination of volume scattering in some urban areas. The negative power problem was identified by van Zyl *et al.* [13] in their model-based decompositions, where they noticed that some single-bounce scattering may have negative power. In our decomposition, which is also model based, we found a similar negative power problem. Our formulation includes the addition of a new model to extract the double-bounce component in the cross-pol, and consequently, the negative power problem can be decreased in most areas. Because the power of each component is determined with (11), the overestimation of the initial component can cause negative power in the rest of the scattering components. Although the negative power was forced to be applied using the previous three-component decomposition algorithm, the negative power problem should be resolved with further improvements of the scattering model or considering propagation factor in the scattering model. The second limitation of the algorithm is still high volume scattering that is found in urban areas where the street orientation is diagonal to the radar illumination direction. Although the extraction of the double-bounce scattering component from the cross-pol signal reduced the volume scattering component, the decomposition color composite image of the San Francisco area still shows a strong volume scattering in some urban areas Fig. 7(c). Solving this excessive volume scattering problem requires further study of radar signal interaction with diagonally oriented buildings.

VI. Conclusion

In this paper, we have used quad-pol C-band RADARSAT-2 data to explore the behavior of co- and cross-pol scattering behaviors in multipath wetland and urban environments. Interferometric processing of the wetland data shows that all four quad interferograms present similar fringe patterns reflecting water-level changes in the wetlands. Because the cross-pol signal clearly indicates scattering from the ground, we suggest that the cross-pol signal includes contributions from both volume and double-bounce scattering and not only volume scattering as commonly assumed. We used this new understanding to propose a modified scattering decomposition approach based on the coherency matrix that decomposes quad-pol data into four components: single bounce, co- and cross-pol double bounce, and volume scattering.

We have applied the new decomposition to two study areas: first to the urban environment of San Francisco area and the other to the rural Everglades wetlands of South FL. The new decomposition results show a very good fit between volume scattering and open areas, such as city parks, in San Francisco. It also shows that a significant part of the cross-pol signal in the urban area consists of double-bounce scattering from building oriented diagonally to the radar direction of illumination. In the wetland environment, the double-bounce component was extracted from the cross-pol showing the variation according to the characteristics of surface's vegetation. The decomposition of the cross-pol signal into volume and double-bounce components can improve SAR-based biomass estimates, which typically assume that the cross-pol signal solely reflects volume scattering.

Acknowledgment

The authors would like to thank the two anonymous reviewers and the Editor for their invaluable comments that greatly improved this paper and JAXA for access to Jers-1 data. This work was enabled by the SOAR project from CSA for access to the RADARSAT-1/2 data.

References

[1] S. R. Cloude and E. Pottier, "A review of target decomposition theorems in radar polarimetry," *IEEE Trans. Geosci. Remote Sens.*, vol. 34, no. 2, pp. 498–518, Mar. 1996.

[2] ESA, PolSARpro. [Online]. Available: http://earth.esa.int/polsarpro/

[3] A. Freeman and S. L. Durden, "A three-component scattering model for polarimetric SAR data," *IEEE Trans. Geosci. Remote Sens.*, vol. 36, no. 3, pp. 963–973, May 1998.

[4] E. Krogager and Z. H. Czyz, "Properties of the sphere, diplane, helix decomposition," in *Proc. 3rd Int. Workshop on Radar Polarimetry (JIPR)*, Nantes, France, Apr. 1995, pp. 106–114, IRESTE, Univ.

[5] J. Nakamura, K. Aoyama, M. Ikarashi, Y. Yamaguchi, and H. Yamada, "Coherent decomposition of fully polarimetric FM-CW radar data," *IEICE Trans. Commun.*, vol. E91b, no. 7, pp. 2374–2379, Jul. 2008.

[6] R. Touzi, A. Deschamps, and G. Rother, "Phase of target scattering for wetland characterization using polarimetric C-band SAR," *IEEE Trans. Geosci. Remote Sens.*, vol. 47, no. 9, pp. 3241–3261, Sep. 2009.

[7] Y. Yamaguchi, T. Moriyama, M. Ishido, and H. Yamada, "Four-component scattering model for polarimetric SAR image decomposition," *IEEE Trans. Geosci. Remote Sens.*, vol. 43, no. 8, pp. 1699–1706, Aug. 2005.

[8] Y. Yamaguchi, Y. Yajima, and H. Yamada, "A four-component decomposition of PolSAR images based on the coherency matrix," *IEEE Geosci. Remote Sens. Lett.*, vol. 3, no. 3, pp. 292–296, Jul. 2006.

[9] Y. Yamaguchi, A. Sato, W.-M. Boerner, R. Sato, and H. Yamada, "Four-component scattering power decomposition with rotation of coherency matrix," *IEEE Trans. Geosci. Remote Sens.*, vol. 49, no. 6, pp. 2251–2258, Jun. 2011.

[10] J. S. Lee and T. L. Ainsworth, "The effect of orientation angle compensation on coherency matrix and polarimetric target decompositions," *IEEE Trans. Geosci. Remote Sens.*, vol. 49, no. 1, pp. 53–64, Jan. 2011.

[11] S. Cloude, *Polarisation: Applications in Remote Sensing*. New York, NY, USA: Oxford University Press, 2009.

[12] J. S. Lee and E. Pottier, *Polarimetric Radar Imaging: From Basics to Applications*. Boca Raton, FL, USA: CRC, 2009.

[13] J. J. van Zyl, M. Arii, and K. Yunjin, "Model-based decomposition of polarimetric SAR covariance matrices constrained for nonnegative eigenvalues," *IEEE Trans. Geosci. Remote Sens.*, vol. 49, no. 9, pp. 3452–3459, Sep. 2011.

[14] M. Neumann, "Remote sensing of vegetation using multi-baseline polarimetric SAR interferometry: Theoretical modeling and physical parameter retrieval," Ph.D. dissertation, Univ. Rennes, Rennes, France, 2009.

[15] M. Neumann, L. Ferro-Famil, and E. Pottier, "A general model-based polarimetric decomposition scheme for vegetated areas," presented at the Proc. International Workshop Science Applications SAR Polarimetry Polarimetric Interferometry (POLINSAR), Frascati, Italy, 2009.

[16] M. Arii, J. J. van Zyl, and K. Yunjin, "A general characterization for polarimetric scattering from vegetation canopies," *IEEE Trans. Geosci. Remote Sens.*, vol. 48, no. 9, pp. 3349–3357, Sep. 2010.

[17] M. Arii, J. J. van Zyl, and K. Yunjin, "Adaptive model-based decomposition of polarimetric SAR covariance matrices," *IEEE Trans. Geosci. Remote Sens.*, vol. 49, no. 3, pp. 1104–1113, Mar. 2011.

[18] A. Sato, Y. Yamaguchi, G. Singh, and S.-E. Park, "Four-component scattering power decomposition with extended volume scattering model," *IEEE Geosci. Remote Sens. Lett.*, vol. 9, no. 2, pp. 166–170, Mar. 2012.

[19] S. H. Hong and S. Wdowinski, "Evaluation of the quad-polarimetric RADARSAT-2 observations for the wetland InSAR application," *Can. J. Remote Sens.*, vol. 37, no. 5, pp. 484–492, Oct. 2011.

[20] D. E. Alsdorf, J. M. Melack, T. Dunne, L. A. Mertes, L. L. Hess, and L. C. Smith, "Interferometric radar measurements of water level changes on the Amazon flood plain," *Nature*, vol. 404, no. 6774, pp. 174–177, Mar. 9, 2000.

[21] S. Wdowinski, F. Amelung, F. Miralles-Wilhelm, H. Dixon, and R. Carande, "Space-based measurements of sheet-flow characteristics in the Everglades wetland, Florida," *Geophys. Res. Lett.*, vol. 31, no. 15, pp. L15503-1–L15503-5, Aug. 2004.

[22] S. Wdowinski, S.-W. Kima, F. Amelunga, T.H. Dixona, F. Miralles-Wilhelmb, and R. Sonenshein, "Space-based detection of wetlands' surface water level changes from L-band SAR interferometry," *Remote Sens. Environ.*, vol. 112, no. 3, pp. 681–696, Mar. 18, 2008.

[23] J. A. Richards, P. W. Woodgate, and A. K. Skidmore, "An explanation of enhanced radar backscattering from flooded forests," *Int. J. Remote Sens.*, vol. 8, no. 7, pp. 1093–1100, Jul. 1987.

[24] S.-H. Hong, S. Wdowinski, and S.-W. Kim, "Evaluation of TerraSAR-X observations for wetland InSAR application," *IEEE Trans. Geosci. Remote Sens.*, vol. 48, no. 2, pp. 864–873, Feb. 2010.

[25] S.-H. Hong, S. Wdowinski, S.-W. Kim, and J.-S. Won, "Multi-temporal monitoring of wetland water levels in the Florida Everglades using interferometric synthetic aperture radar (InSAR)," *Remote Sens. Environ.*, vol. 114, no. 11, pp. 2436–2447, Nov. 15, 2010.

[26] B. R. N. Gondwe, S.-H. Hong, S. Wdowinski, and P. Bauer-Gottwein, "Hydrologic dynamics of the groundwater-dependent Sian Ka'aN wetlands, Mexico, from InSAR and SAR data," *Wetlands*, vol. 30, no. 1, pp. 1–13, Feb. 2010.

[27] Z. Lu and O. I. Kwoun, "RADARSAT-1 and ERS InSAR analysis over southeastern coastal Louisiana: Implications for mapping water-level changes beneath swamp forests," *IEEE Trans. Geosci. Remote Sens.*, vol. 46, no. 8, pp. 2167–2184, Aug. 2008.

[28] S.-H. Hong, S. Wdowinski, and S. Kim, "Space-based water level observation of the Everglades from dual polarization InSAR data," in *AGU Fall Meeting*, San Francisco, CA, U.S.A., 2008.

[29] S.-H. Hong, S. Wdowinski, and S.-W. Kim, "Wetland InSAR over the Everglades from space observed polarimetric data," in *Proc. POLinSAR*, Frascati, Italy, 2009.

[30] S. M. Buckley *et al.*, ROI_PAC Documentation - Repeat Orbit Interferometry Package. 2000.

[31] R. M. Goldstein and C. L. Werner, "Radar interferogram filtering for geophysical applications," *Geophys. Res. Lett.*, vol. 25, no. 21, pp. 4035–4038, Nov. 1, 1998.

[32] I. Hajnsek, K. Papathanassiou, T. Busche, T. Jagdhuber, J. Kim, M. S. Ferrer, S. Sauer, and M. Villano, "Fully polarimetric TerraSAR-X data: Data quality and scientific analysis," in *Proc. IGARSS*, 2010.
[33] U. Soergel, E. Cadario, H. Gross, A. Thiele, and U. Thönnessen, "Bridge detection in multi-aspect high-resolution interferometric SAR data," in *Proc. EUSAR*, 2006.
[34] J. Lee, "Interpreting off-diagonal terms in polarimetric coherency matrix," in *Proc. IEEE IGARSS*, 2001, pp. 913–915.

Sang-Hoon Hong (S'03–M'07) received the B.S. and M.S. degrees in geological sciences and the Ph.D. degree in earth system sciences from Yonsei University, Seoul, Korea, in 1997, 1999, and 2006, respectively.

He is currently a Senior Researcher with the Satellite Information Research Center, Korea Aerospace Research Institute, Daejeon, Korea. He was a Postdoctoral Researcher with the Division of Marine Geology and Geophysics, University of Miami, Miami, FL, USA, and also with the College of Engineering and Computing, Florida International University, Miami, FL, USA. He is a Principal Investigator of projects supported by the German Space Agency and Japan Aerospace Exploration Agency for research using synthetic aperture radar (SAR) observations. His research interests include radar interferometry, radar polarimetry, and microwave signal processing. He applied these SAR, interferometric SAR, and polarimetric SAR techniques for the study of geophysical parameter retrieval and geodetic change observation.

Shimon Wdowinski received the B.Sc. degree in earth sciences and the M.Sc. degree in geology from Hebrew University, Jerusalem, Israel, in 1983 and 1985, respectively, and the M.S. degree in engineering sciences and the Ph.D. degree in geophysics from Harvard University, Boston, MA, USA, in 1988 and 1990, respectively.

He is currently a Research Associate Professor with the Division of Marine Geology and Geophysics, Rosenstiel School of Marine and Atmospheric Science, University of Miami, Miami, FL, USA. He is a Principal Investigator of projects funded by NASA, European Space Agency, Canadian Space Agency, German Space Agency, and Italian Space Agency on studies using synthetic aperture radar (SAR) and interferometric SAR observations for wetland research. His research has focused on the development and usage of space geodetic techniques that can detect very precisely small movements of the Earth's surface. He successfully applied these technologies to study natural hazards and environmental phenomena, such as earthquakes, sea-level rise, landslides, urban subsidence, and wetland surface flow.